

Programmable Shaping of Femtosecond Optical Pulses by Use of 128-Element Liquid Crystal Phase Modulator

Andrew M. Weiner, *Senior Member, IEEE*, Daniel E. Leaird, J. S. Patel, and John R. Wullert, II

Abstract—We describe programmable shaping of femtosecond pulses by using a 128-element liquid crystal modulator to manipulate the phases of optical frequency components which are spatially dispersed within a grating-and-lens pulse shaping apparatus. Our apparatus makes possible gray-level control of the spectral phases and allows modification of the pulse shape on a millisecond time scale under electronic control. Refinements in the design of the multielement modulator result in pulse shaping fidelity comparable to that which can be achieved with microlithographically fabricated masks. Several examples of pulse shaping operation, including pulse position modulation, programmable pulse compression, and adjustable cubic phase distortion, are described. Broad limitations imposed by the fixed modulator geometry are analyzed.

I. INTRODUCTION

OVER the last several years a growing interest in controlling the shapes of ultrashort optical pulses has emerged, and several techniques for tailoring pulse shapes have now been demonstrated [1]–[7]. The ability to synthesize ultrashort pulse waveforms to specification has opened up a number of new applications areas for ultrashort optical pulses. Pulse shaping techniques have been utilized for generation of coded trains of femtosecond pulses for high-speed communications [3], [8], for studies of soliton propagation in fibers [9]–[11], and for experimental demonstrations of all-optical switching [12], [13]. Applications of specially shaped femtosecond pulses for time-resolved spectroscopy and control of molecular motion have been proposed [11], [14], [15] and demonstrated [16]. Pulse tailoring techniques have also been applied to measure the phase and intensity profile of ultrashort pulses [17], [18], to generate extremely high rate pulse trains [19], [20], to optimize pulse compression experiments [21], [22], to achieve tunable spectral filtering of femtosecond white-light continuum [23], and to compensate for the effects of cubic phase distortion [24], [25]. Further applications of pulse shaping can be anticipated throughout the field of ultrafast optics.

The techniques reported for shaping ultrashort optical pulses may generally be thought of as Fourier transform techniques, in which pulse shaping is achieved through

manipulation in the frequency domain. The most widely utilized technique achieves pulse shaping by linear filtering of optical frequency components which are spatially dispersed within a simple lens and grating apparatus [1], [3], [4]. By utilizing fixed, microlithographically-fabricated, spatial masks to manipulate the amplitudes and phases of spatially dispersed frequency components, incident femtosecond pulses can be reshaped with high precision into waveforms with envelopes greater than 10 ps in duration and with individually controllable features shorter than 100 fs in duration [4]. We recently reported an extension of this technique in which a 32-element liquid crystal phase modulator was utilized in place of a pre-fabricated spatial mask in order to achieve electronically programmable femtosecond pulse shaping [26]. In this paper we describe programmable shaping of femtosecond pulses by using a new, 128-element liquid crystal phase modulator which provides substantially improved spectral resolution compared to the original 32-element phase modulator. This increase in spectral resolution makes possible synthesis of ultrashort pulse waveforms of a complexity previously possible only with the microlithographically fabricated masks. Refinements in the design of the pulse shaping apparatus and the modulator itself have resulted in improved pulse shaping fidelity. Thus, this apparatus now provides electronically controllable waveform selection and continuously variable phase control as well as excellent spectral resolution and pulse shaping quality.

The remainder of this paper is structured as follows. The pulse shaping apparatus, including design and packaging of the liquid crystal phase modulator, is described in Section II. Examples of programmable pulse shaping using binary control of the optical phases are reported in Section III. Section IV deals with programmable pulse shaping utilizing continuously variable (or gray-level) phase control. In particular, we demonstrate the use of the multielement phase modulator to achieve femtosecond pulse position modulation and programmable femtosecond pulse compression and to impart adjustable cubic phase sweeps onto femtosecond pulses. Included in this section is a discussion of the effect of the fixed size of the modulator elements on pulse shaping operation. In Section V we conclude.

Manuscript received July 2, 1991.
The authors are with Bellcore, Red Bank, NJ 07701.
IEEE Log Number 9106658.

II. EXPERIMENTAL APPARATUS

Our programmable pulse shaping apparatus, shown schematically in Fig. 1, is similar to our previous pulse shaping setup using fixed masks [4]. A colliding-pulse mode-locked (CPM) dye laser [27] provides 75 fs duration pulses, centered at a wavelength of $0.62 \mu\text{m}$, which serve as the input to the shaper. After striking the first grating, the frequency components that make up the incident pulse spread out to different spatial positions. The first lens focuses these frequency components to separate spots at the filter plane where the liquid crystal phase modulator is located. The second lens and grating recombine each of the separate frequency components into a single output beam. For reasons which will be discussed below, the liquid crystal modulator is designed to operate with a vertically polarized input beam. Since a horizontal input polarization is required for good diffraction efficiency from the gratings, a pair of zero-order half-wave plates is inserted before and after the liquid crystal modulator. The first half-wave plate rotates the input polarization by 90° in order to obtain the required vertical polarization for the modulator, and the second wave plate rotates the polarization back to horizontal in order to match the second diffraction grating.

The gratings have 1800 lines/mm and are used at close to the Littrow angle; the lenses are achromats with 15 cm focal lengths. The distances between gratings and lenses in the pulse shaper are set for zero net temporal dispersion [1], [28]. Therefore, when the liquid crystal modulator is turned off, the temporal shape of the output pulse is the same as that of the input. When the modulator is active, it modifies the output pulse shape by adjusting the phases of separate frequency components corresponding to distinct control elements (pixels). The output temporal profile is determined by the Fourier transform of the pattern transferred by the multielement modulator onto the spectrum. The output intensity profile is measured by cross-correlating the output with an unshaped reference pulse. Compared to fixed masks, the liquid crystal modulator allows continuously variable gray-level phase control of each separate pixel (whereas the fixed masks provided only binary phase control). Furthermore, the multielement phase modulator makes possible electronically programmable control of the pulse shape and allows modulation of the pulse shape on a millisecond time scale under computer control.

A schematic of the multielement liquid crystal phase modulator is shown in Fig. 2. An approximately $4 \mu\text{m}$ thick liquid crystal layer (type 'E7' nematic liquid crystal from British Drug House) is sandwiched between two pieces of glass. The inside surface of each piece of glass is coated with a thin, transparent, electrically conducting film of indium tin oxide (ITO). The back piece of glass has a continuous layer of ITO that acts as a ground plane. The front half is patterned into 128 separate electrodes (or pixels) with the corresponding fan-out for electrical connections. The pixel spacing is $40 \mu\text{m}$ center to center with

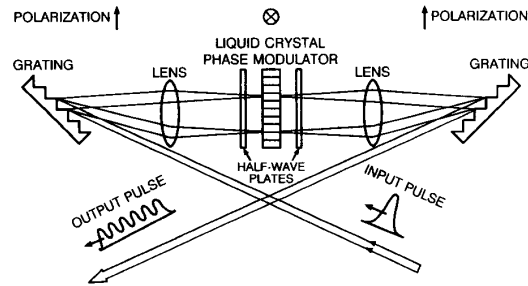


Fig. 1. Top view of the programmable femtosecond pulse shaping apparatus. The lens pair forms a unit magnification telescope, and the gratings are placed in the outside focal planes of the lenses.

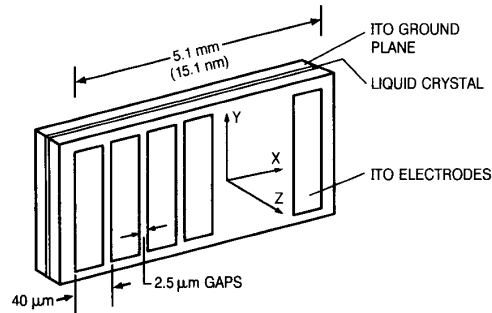


Fig. 2. Schematic diagram of the 128-element liquid crystal phase modulator. The indium-tin-oxide (ITO) electrodes and ground plane are actually on the inside surface of the two pieces of glass.

$2.5 \mu\text{m}$ gaps between pixels, and the active region is $500 \mu\text{m}$ high. Because the $40 \mu\text{m}$ pixel size is nearly as small as the focused spot size of individual optical frequency components (approximately $25 \mu\text{m}$), the multielement modulator effectively utilizes the spectral resolution available from our apparatus. The number of pixels (128) was selected so that the total aperture (5.12 mm) accommodates the entire spatially dispersed frequency spectrum.

A cross-sectional view of the modulator is shown in Fig. 3. The liquid crystal layer is composed of long, thin, rod-like molecules. The device is fabricated so that with no applied electric field, the liquid crystal molecules are aligned with their long axes along the y direction (see Fig. 3). When an electric field is applied (in the z direction), the liquid crystal molecules tilt along z , causing a refractive index change for y -polarized light. The maximum available phase change is given by $|\Delta\phi| = 2\pi\Delta nL/\lambda$, where Δn and L are, respectively, the birefringence and the thickness of the liquid crystal layer. For our device, with $\Delta n \approx 0.225$ and $L \approx 3.5 \mu\text{m}$, the maximum phase change is approximately 2.5π . We note that in the gap regions between pixels, the phase is affected only by the fringing fields from the neighboring electrodes. The discontinuities associated with the gaps can cause scattering which degrades the shaped pulses. To minimize this effect, we made the gaps as small as our photolithography process would conveniently allow.

There are two main differences between the current

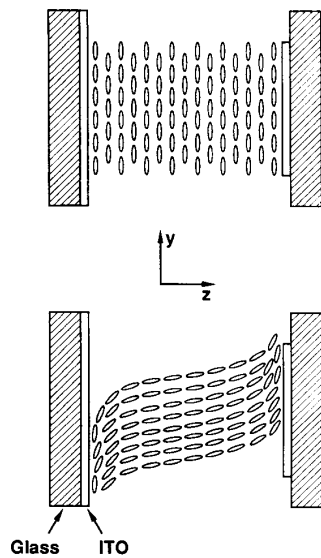


Fig. 3. Cross-sectional view of the multielement modulator. With no electric field, the liquid crystal molecules are aligned along y ; when an electric field is applied (along z), the molecules tilt along z , causing a refractive index change for y -polarized light.

128-element liquid crystal phase modulator and the 32-element modulator reported previously [26]. First, the physical layout is modified so that the 128-element modulator has smaller gap regions between elements and accommodates the entire optical bandwidth. The second, more fundamental difference is the liquid crystal orientation. In the original 32-element modulator with no applied field, the liquid crystal molecules were oriented along x in order to match the preferred polarization of the gratings in the pulse shaper. In the new 128-element modulator, the orientation was modified in order to minimize edge effects, as discussed below.

Fig. 4 shows photographs of a section of the active region of the original 32-element and the current 128-element modulator. The photos were taken using a polarizing microscope with every other pixel activated. A substantial difference in the edge effects is evident; in particular, the optical response in the vicinity of the gap regions is much more uniform for the 128-element modulator than for the 32-element modulator. In order to explain the difference, we consider a single pixel in the presence of an electric field along z . With the default liquid crystal orientation along x (corresponding to the 32-element modulator design), the direction of the liquid crystal long axis changes from along x in the gap region to along z in the electroded region. This causes splay-bend deformation [29] in the vicinity of the electrode edge. Since the elastic constants for this type of deformation are larger than those for the twist deformation, the structure spontaneously relaxes to one which decreases the splay-bend deformation at the cost of increased twist deformation. Such structural changes have been observed previously in polymeric liquid crystal systems [30]. A way

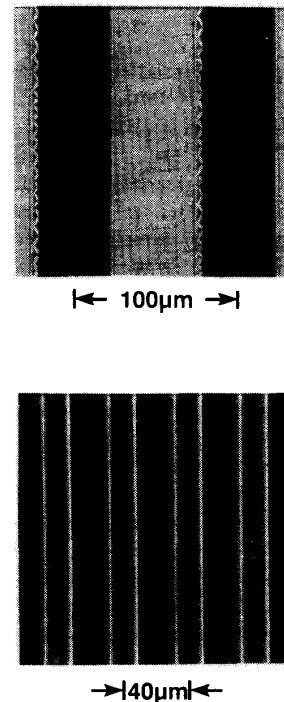


Fig. 4. Photographs of a section of the active region of the original 32-element modulator (top) and the current 128-element modulator (bottom). The photos were taken with a polarizing microscope with every other pixel activated. The 128-element modulator is evidently much more regular.

to avoid this instability is to use a geometry in which only the twist deformation occurs when an electric field is applied. This is achieved by aligning the liquid crystal along y (corresponding to the design of our 128-element modulator). This geometry requires a 90° polarization rotation within the pulse shaper, which is accomplished by using the half-wave plates shown in Fig. 1. The improvement in pulse shaping quality resulting from the geometry change will be seen quite clearly in Section IV below.

One of the major issues in implementing the 128-element modulator was packaging. In order to make reliable electrical connections to the device, we utilized a commercial leadless chip carrier socket, which we modified to suit our needs. Fig. 5 shows the final packaging scheme—partially disassembled for the photo. The steel cover plate (right-hand side of the photo) is used to clamp the modulator into place on the modified socket. Metal-on-elastomer (MOE) connectors are used between the modulator and the socket to enhance electrical contact, and between the modulator and the steel cover plate to reduce stress on the glass. The connections from the socket are fanned out on a P.C. board to ribbon cable connections (reverse side). Ribbon cables are then used to connect the modulator to the driving electronics. Although the uniformity of the modulator array was found to be quite good (see Section IV-A below), the electrical

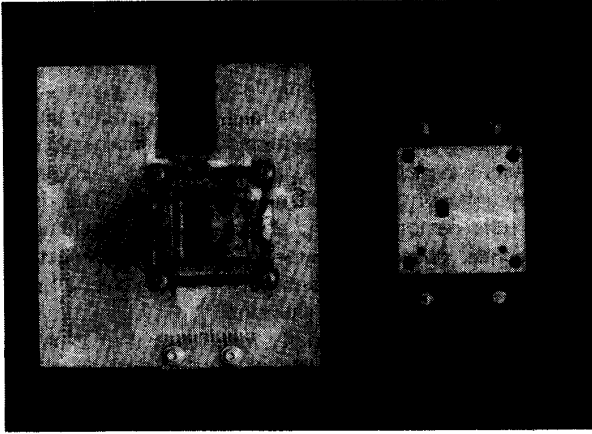


Fig. 5. Photograph of the packaged multielement modulator, partially disassembled for the photo.

connections to a few of the modulator elements (typically three) were found to be open circuits. These faults were caused either by breaks on the ITO lines on the liquid crystal modulator itself or by unsuccessful contacts between the modulator array and the chip carrier. The number of faults was sufficiently small that pulse shaping operation was not noticeably affected.

In order to provide independent gray-level control of the phase of each pixel in the 128-element modulator, we designed and constructed a special drive circuit. The driver circuit generates 128 separate, variable-amplitude, 200 Hertz bipolar square waves to control each pixel. The phase change is controlled by the amplitude of the applied voltage; the 200 Hertz bipolar square wave does not directly affect the phase but is required to prevent electro-migration effects in the liquid crystal. The electronics consist of eight 8-bit digital-to-analog converters (DAC's) combined with eight, 16-channel, analog multiplexors. Each output is thus driven for only 1/16 of the time (time-multiplexing); a 2200 pF capacitor is placed in parallel with each pixel in order to hold the voltage between refresh cycles. The digital input data for the DAC's is loaded into local memory from a personal computer, thus facilitating the generation of complex phase patterns. For a given digital input, the voltages generated on the 128 output lines are uniform to $\pm 1.5\%$, with the differences being primarily due to electrical crosstalk between the multiplexed lines.

III. BINARY PHASE CONTROL

As an initial test of the 128-element modulator, we demonstrated pulse shaping under binary phase control. Each modulator element could be set independently to either of the two programmed levels V_1 and V_2 , corresponding to two different phases ϕ_1 and ϕ_2 . Usually (but not always) one of the voltages was set to zero, and the phase difference $\Delta\phi = \phi_1 - \phi_2$ was set to π . In order to determine voltage settings corresponding to a π phase dif-

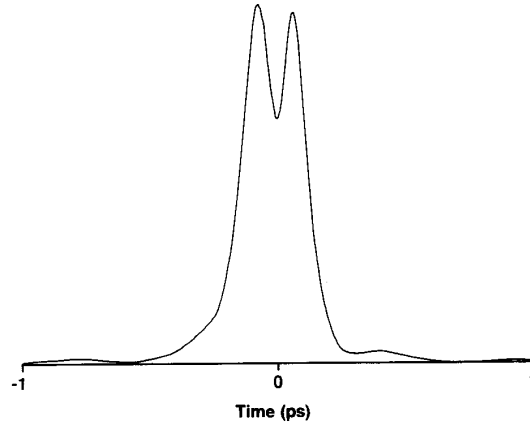


Fig. 6. Cross-correlation measurement of a femtosecond odd pulse.

ference, we first generated femtosecond odd pulses [2], [4]. The odd pulse arises when half of an originally symmetric spectrum undergoes a π phase shift, thereby becoming an antisymmetric spectrum. The resulting electric field is an odd function of time, with an intensity profile consisting of two peaks separated by a null at $t = 0$, where the phase of the carrier jumps abruptly by π . Such odd pulses are closely related to zero-area pulses produced by propagation through resonant atomic vapors [31]. A cross-correlation measurement of a fs odd pulse is plotted in Fig. 6. Two peaks, spaced by ≈ 135 fs, are clearly evident, although the individual peaks are only partially resolved due to the 75 fs duration of the reference pulse. The relative heights of the two main intensity peaks are a sensitive function of the relative phase $\Delta\phi$. When $\Delta\phi = \pi$, as in the figure, the two main peaks are close to equal. On the other hand, when $\Delta\phi$ is slightly less than π or slightly greater than π , the intensities of the two peaks become markedly asymmetric. In our experiments generation of femtosecond odd pulses provides a simple method for adjusting the multielement modulator for a π relative phase shift. This technique also provides a straight-forward check for the complete, gray-level phase calibration described in Section IV below.

In addition to the odd pulse, other examples of pulse shaping using binary phase control are readily achieved simply by reprogramming the modulator. Two further examples are shown in Fig. 7. The data plotted in Fig. 7(a) result when the phases of the individual pixels alternate periodically between zero and π , according to the pattern $\{0000\pi\pi\pi\pi0000\pi\pi\pi\pi \dots\}$. The waveform consists of two main pulses, separated by 2.7 ps, together with a series of several weaker pulses, separated by additional multiples of 2.7 ps from the main peaks. The data are in good agreement with the theoretical intensity profile, Fig. 7(b). The apparent difference in the pulsewidths arises because Fig. 7(a) represents a cross-correlation measurement while Fig. 7(b) shows the raw intensity. A second noticeable difference is the weak pulse at $t = 0$ in the experimental trace, which is not present in Fig. 7(b). The

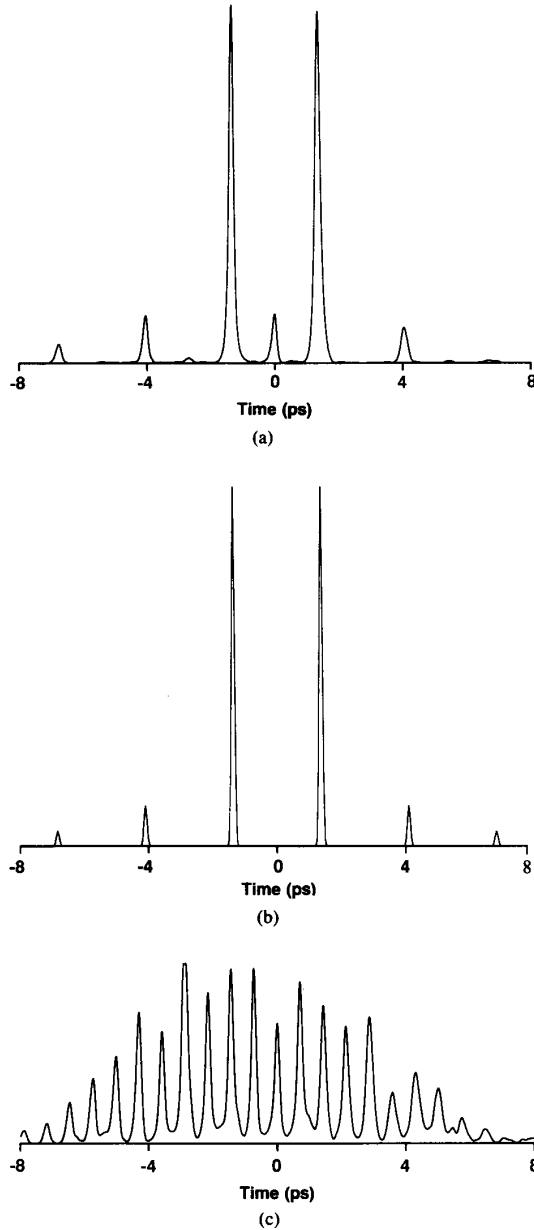


Fig. 7. Examples of pulse shaping using binary phase control. (a) Cross-correlation measurement of a pulse doublet resulting when the phases alternate periodically between 0 and π . (b) Theoretical intensity profile corresponding to (a). (c) Cross-correlation measurement of a 1.39 THz pulse train generated using binary phase control.

field amplitude at $t = 0$ is expected to be proportional to the area under the masked spectrum $E(\omega)$. In the calculation the field is zero at $t = 0$, since the spectrum has zero integrated area (assuming a symmetric input spectrum). The weak pulse present at $t = 0$ in the experiment results from the slightly nonsymmetric spectrum of the actual input pulses. Fig. 7(c) shows a series of approximately twenty evenly-spaced pulses, repeating with a pe-

riod of 1.39 THz and filling most of a 16 ps window. The pulse sequence is formed by setting the phases of the modulator pixels according to periodic repetitions of a length-15 pseudorandom sequence, given by $\{000\pi00\pi\pi0\pi0\pi\pi\pi\}$. Generation of such periodic pulse trains by using periodic, pseudorandom-sequence, phase-only filters was demonstrated previously with fixed, microlithographically patterned masks [4], [19]. The data plotted here demonstrate the ability of the 128 element liquid crystal phase modulator to provide high spectral resolution sufficient to perform pulse shaping over a time window exceeding 10 ps in duration.

For completeness, we briefly mention real-time pulse shaping operation. An example of real-time pulse shaping was shown in [26] for the 32-element phase modulator. The data demonstrated complete switching from a single pulse to a pulse doublet [of the type shown above in Fig. 7(a)] within 25 ms. The actual turn-on and turn-off times measured for the 32-element modulator were 2 ms and 20 ms, respectively (although the switching times do depend on the bias voltage levels). Similar switching times and real-time pulse shaping capability are expected with the 128-element modulator. Faster switching times, down to microsecond time scales, should be possible using ferroelectric liquid crystals, particularly for binary phase modulation.

IV. CONTINUOUSLY VARIABLE PHASE CONTROL

In this section we discuss operation of the modulator under gray-level phase control, in which the phase of each modulator element can be adjusted continuously and independently over the range of 0 to 2π . Compared to our previous utilization of microlithographically defined masks, which provided only binary phase levels (usually 0 or π), continuously variable phase control allows more general pulse shaping applications. We first discuss the phase versus voltage calibration of the modulator, which is necessary in order to accomplish gray-level control, and comment on the uniformity of the modulator array. We then present several applications of gray-level phase control. In particular, we use the modulator array to impart linear, quadratic, and cubic phase sweeps onto the optical frequency spectrum. These phase sweeps correspond in the time domain, respectively, to pulse position modulation, to programmable chirping and pulse compression, and to a complex pulse distortion. These examples will serve to demonstrate the ability to impress nearly arbitrary phase modulations onto the frequency spectrum. We will also discuss one limitation of the multielement modulator, namely, the effect of the fixed $40\text{ }\mu\text{m}$ size of the individual modulator elements on the range of shaped pulses which can be achieved.

A. Phase Versus Voltage Calibration

In order to accomplish gray-level phase control, it is first necessary to calibrate the phase response of the modulator as a function of applied voltage. In our previous

work with the 32-element modulator, we had performed the calibration with the multielement modulator in the pulse shaper, by observing shifts of the temporal beat note between two isolated frequency components as a function of applied voltage to the modulator [26]. For the present paper, we performed the calibration by using a different and simpler procedure, in which we removed the modulator from the pulse shaping apparatus, and set it up to operate as an amplitude modulator for a HeNe laser. The HeNe laser is linearly polarized, with its polarization rotated 45° relative to the alignment direction of the liquid crystal. The laser beam is focused onto a single pixel of the multielement modulator, and the transmission through a subsequent crossed polarizer is recorded as a function of applied voltage. The phase calibration is obtained from the transmission versus voltage curve by using the relation

$$T(V) = \sin^2 \left(\frac{\phi_y(V) - \phi_x}{2} \right) \quad (1)$$

where $T(V)$ is the fractional transmission through the crossed polarizer, and V is the applied voltage. $\phi_y(V)$ and ϕ_x are the phases imposed by the modulator on light polarized along the y and x polarizations, respectively. ϕ_x corresponds to light polarized along the short axis of the liquid crystal molecules and for any particular pixel is independent of the applied voltage. Note, however, that ϕ_x can vary from pixel to pixel, since the thickness of the liquid crystal layer can vary slightly across the modulator. $\phi_y(V)$ is a function of voltage and corresponds to the phase which will be imposed by the modulator onto the optical spectrum when the modulator is placed within the pulse shaper. If we define $\phi_y(V) = -2\pi n_{\text{eff}}(V)L/\lambda$, where $n_{\text{eff}}(V)$ is the effective index for y -polarized light, then $\phi_y(V)$ increases as the voltage is raised, since n_{eff} decreases. In the limit $V \rightarrow \infty$, the liquid crystal molecules will align completely along the z axis; therefore, x - and y -polarized light will see the same effective refractive index. Consequently, for any given pixel, $\phi_y(V \rightarrow \infty) = \phi_x$.

In order to test the uniformity of the multielement modulator, we measured a series of calibration curves corresponding to different modulator pixels. Good uniformity across the array is required for precise pulse shaping control. Fig. 8(a) shows three representative calibrations—one taken each 2.5 mm across the modulator. The vertical axis represents the change in phase as a function of voltage, relative to the phase at that pixel for zero voltage. The shapes of the calibrations are quite similar, indicating good uniformity across the array. The phase is constant for voltages below a threshold voltage of ≈ 0.9 V. Above the threshold voltage the phase change increases rapidly at first, then more slowly as the phase change begins to saturate above ≈ 2.5 V. The total phase change varies slightly across the modulator, ranging from 2.38π on one end of the modulator to 2.50π on the other. Because the total phase change is easily greater than 2π , full gray-

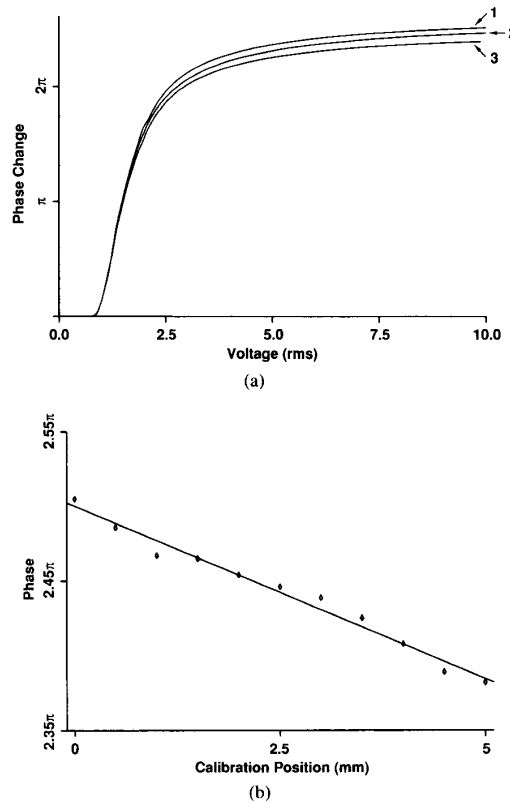


Fig. 8. (a) Series of three phase vs. voltage calibrations, one taken each 2.5 mm across the modulator. (b) Phase variation across the modulator, measured at a constant voltage level of 10 V rms. Curves labeled 1, 2, and 3 in (a) correspond to positions 0, 2.5, and 5.0 mm, respectively, in (b).

level phase control can be achieved. The variation in phase across the modulator, measured at a constant voltage level of 10 V rms, is plotted in detail in Fig. 8(b). Also plotted is a straight line fit which evidently matches the data quite well. We attribute this gradient in the phase change to a variation in the modulator thickness. Given the birefringence $\delta n = 0.225$ of the liquid crystal and the He-Ne wavelength $0.6328 \mu\text{m}$, we estimate that the actual thickness varies from 3.35 to $3.52 \mu\text{m}$. Note that this thickness variation, to the extent that it is linear, does not adversely affect the quality of shaped pulses; a linear phase variation in the frequency domain simply advances or delays the pulse in the time domain. The deviation of the phase variation from linearity, as shown in Fig. 8(b), is approximately 0.016 rad rms, which is better than the uniformity of the driving electronics used for the pulse shaping. Thus, a single calibration curve is sufficient to represent the phase response of the entire modulator array. For the work described below on gray-level phase control, the calibration curve corresponding to the physical center of the modulator array was stored on the personal computer. The phase values shown in Fig. 8 were multiplied by a factor of 1.02 to account for the difference between the CPM laser center wavelength of $0.62 \mu\text{m}$ and the $0.6328 \mu\text{m}$ calibration wavelength.

B. Pulse Position Modulation

We have utilized gray-level control of the optical phase to achieve femtosecond pulse position modulation (PPM). We rely on the fact that if $f(t)$ and $F(\omega)$ are a Fourier transform pair, then the delayed signal $f(t - \tau)$ is the Fourier transform of $F(\omega) \exp(-i\omega\tau)$. Thus a pulse can be retarded (or advanced) by imposing a linear phase sweep onto its spectrum. The delay τ is given by the relation

$$\tau = -\delta\phi/2\pi\delta f \quad (2)$$

where $\delta\phi$ and δf are, respectively, the imposed phase change per pixel and the change in optical frequency from one pixel to the next. For our setup, δf is approximately 0.092 THz for the 128-element modulator, and therefore $\tau = -10.87(\delta\phi/2\pi)$ ps. (For our original 32-element modulator we had $\delta f = 0.230$ THz and $\tau = -4.34(\delta\phi/2\pi)$ ps.) We note that because of their finite pixel size, our multielement modulators do not precisely produce a linear phase sweep but rather produce a "rectangular approximation" to a linear phase sweep. The effect of this rectangular approximation will be analyzed below.

Fig. 9 shows cross-correlation measurements of temporally shifted pulses achieved by means of pulse position modulation. Data are shown for a phase change per pixel ($\delta\phi$) of 0 and $\pm 0.25\pi$ for both 128- and 32-element phase modulators. In both sets of data, pulses are clearly advanced and retarded. The amount of temporal shift, ± 1.38 ps for the 128-element modulator and ± 0.55 ps for the 32-element modulator, are in close agreement with that expected from (2). The positive phase shift ($+\pi/4$) corresponds to pulses shifted to negative times; the negative phase shift ($-\pi/4$) corresponds to pulses shifted to positive times. Two differences between the data obtained with 128-element modulator and that obtained with the 32-element modulator are apparent. First, the time shift obtained for fixed $\delta\phi$ is $2.5\times$ greater with the 128-element modulator, in agreement with the fact that the pixel size and therefore δf is $2.5\times$ smaller for the 128-element modulator compared to the 32-element modulator. The greater time shift obtained with the 128-element modulator is indicative of the wider temporal window over which pulse shaping may be achieved. Second, for the data obtained with the 32-element modulator, PPM is accompanied by a loss of peak intensity, an increase in energy in the wings, and a slight pulse distortion [26]. These effects arise mainly owing to scattering associated with the $5\text{ }\mu\text{m}$ gaps separating the electrodes. On the other hand, for the data obtained with the 128-element modulator, PPM is achieved essentially without pulse distortion. The enhanced pulse shaping fidelity observed with the 128-element modulator can be attributed to the reduced scattering losses achieved by the smaller $2.5\text{ }\mu\text{m}$ gap dimension and by the improved orientation of the liquid crystal molecules.

The temporal range over which pulse position modulation may be achieved is limited by the requirement that

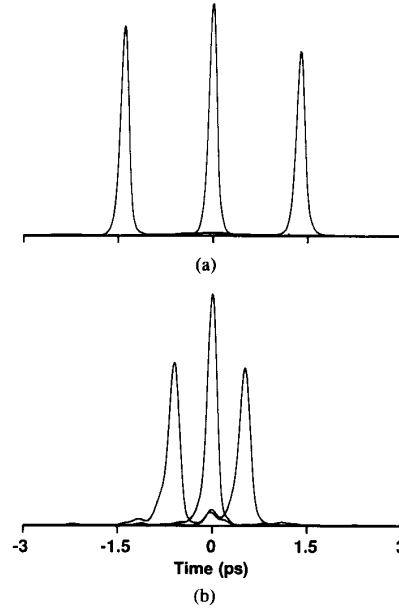


Fig. 9. Cross-correlation measurements of temporally shifted pulses achieved by means of pulse position modulation with $\delta\phi = \pm\pi/4$. Top: Data for the 128-element modulator, showing a time shift of ± 1.38 ps. Bottom: Data for the 32-element modulator, showing a time shift of ± 0.55 ps. The positive phase shift ($+\pi/4$) corresponds to pulses shifted to negative times; the negative phase shift ($-\pi/4$) corresponds to pulses shifted to positive times.

the actual spectral phase modulation approximate a smooth, linear phase sweep, despite the fixed, finite size of the individual modulator elements. Essentially this is a sampling limitation: the phase must vary sufficiently slowly that it is adequately sampled by the fixed modulator elements—i.e., we require $|\delta\phi| \ll \pi$. From (2), then, we find $|\tau| < 1/2\delta f$. In order to understand how the PPM breaks down as we approach $\delta\phi = \pm\pi$ and $\tau = \pm 1/2\delta f$, we now analyze pulse shaping with a multielement modulator, concentrating on the effect of the fixed, finite size of individual modulator elements.

Pulse shaping is most conveniently analyzed in the frequency domain. The spectrum of the pulse emerging from the pulse shaping setup is given by

$$E_{\text{out}}(\omega) = E_{\text{in}}(\omega)M_{\text{eff}}(\omega) \quad (3)$$

where $E_{\text{out}}(\omega)$ and $E_{\text{in}}(\omega)$ are the complex amplitudes of the output and input electric field spectra, respectively, and $M_{\text{eff}}(\omega)$ is the effective frequency filter implemented by a mask or multielement modulator within the pulse shaping setup. The effective frequency filter is related to the physical mask by

$$M_{\text{eff}}(\omega) = \int dx M(x) \exp[-2(x - \alpha\omega)^2/w_0^2] \quad (4)$$

where $M(x)$ represents the complex transmittance of the physical (spatial) mask, α denotes the spatial dispersion

$$\alpha = \left(\frac{d\omega}{dx}\right)^{-1} = \frac{-\lambda^2}{2\pi c} \left(\frac{d\lambda}{dx}\right)^{-1},$$

and w_o is the radius of the electric field spatial profile of an individual frequency component at the masking plane [32]. For our setup $\delta f/\delta x = 2.3$ THz/mm and $\alpha = 6.92 \times 10^{-14}$ mm s. The effective frequency filter $M_{\text{eff}}(\omega)$ is given by the complex transmittance of the physical mask $M(x)$ convolved with the spatial intensity profile of the focused beam. In the case when the physical mask contains features smaller than the spot size w_o , these smaller features will be smeared out by the convolution integral; the finest spectral features present in $M_{\text{eff}}(\omega)$ will be limited by this smearing to a width of order w_o/α . Conversely, when the spot size w_o is substantially smaller than the smallest features on the mask (i.e., when the spectral resolution of the pulse shaping setup exceeds that called for by the mask), the frequency filter is identical in form to the physical mask:

$$M_{\text{eff}}(\omega) \sim M(x/\alpha). \quad (5)$$

For the current experiments, the smallest physical feature is determined by the size of the individual modulator elements (40 μm), and the spot size w_o is of order 15–20 μm . Therefore, to a good approximation, (5) does apply (although the finite spot size will smear out the sharp edges associated with individual modulator elements).

For the multielement modulator, the complex transmittance $M(x)$ can be written

$$M(x) = \left\{ H\left(\frac{x}{\alpha}\right) \sum_{n=-N/2}^{N/2-1} \delta(x - n \delta x) \right\} * \text{rect}\left(\frac{x}{\delta x}\right). \quad (6)$$

$H(\omega)$ represents the desired frequency filtering function—for PPM, for example, $H(\omega)$ will be a continuous linear phase sweep. $\delta(x)$ is the Dirac delta function, δx is the pixel spacing (40 μm in our case), $\text{rect}(x)$ is the unit rectangle function equal to 1 for $|x| \leq \frac{1}{2}$ and equal to 0 for $|x| \geq \frac{1}{2}$, and $*$ denotes convolution. Equation (5) expresses the fact that a multielement modulator provides a sampled version of the desired masking function $H(x/\alpha)$. For small w_o , (5) applies, and the spectral filtering function is given by

$$M_{\text{eff}}(\omega) = \left\{ H(\omega) \sum_{n=-N/2}^{N/2-1} \delta(\omega - n \delta\omega) \right\} * \text{rect}\left(\frac{\omega}{\delta\omega}\right) \quad (7)$$

where $\delta\omega = \delta x/\alpha = 2\pi\delta f$ is the optical frequency bandwidth spanned by a single modulator element.

The shaped pulse in the time domain $e_{\text{out}}(t)$ is obtained from the Fourier transform of (2), as follows:

$$e_{\text{out}}(t) = e_{\text{in}}(t) * m_{\text{eff}}(t). \quad (8)$$

Here $e_{\text{out}}(t)$, $e_{\text{in}}(t)$, and $m_{\text{eff}}(t)$ are the Fourier transforms of $E_{\text{out}}(\omega)$, $E_{\text{in}}(\omega)$, and $M_{\text{eff}}(\omega)$, given for example by

$$m_{\text{eff}}(t) = \frac{1}{2\pi} \int d\omega e^{i\omega t} M_{\text{eff}}(\omega). \quad (9)$$

Physically $e_{\text{out}}(t)$ and $e_{\text{in}}(t)$ are the output and input complex electric field profiles, respectively, and $m_{\text{eff}}(t)$ is the effective impulse response function of the pulse shaper.

Using (6) we find

$$m_{\text{eff}}(t) \sim \left\{ h(t) * \sum_{n=-\infty}^{\infty} \text{sinc}(N\pi\delta f(t - n\delta f^{-1})) \right\} \cdot \text{sinc}(\pi\delta f t) \quad (10)$$

where $h(t)$, the desired impulse response function, is the Fourier transform of $H(\omega)$, and $\text{sinc}(t) = \sin(t)/t$. If, as in the current experiments, the spectral window corresponding to the entire width of the modulator array exceeds the bandwidth of the input spectrum, or equivalently, if $e_{\text{in}}(t)$ is wider than the $\text{sinc}(N\pi\delta f t)$ factor in (9), then the equations can be simplified by replacing the $\text{sinc}(N\pi\delta f t)$ terms by delta functions. In this case we obtain

$$e_{\text{out}}(t) \sim \left\{ e_{\text{in}}(t) * \sum_n h(t - n\delta f^{-1}) \right\} \cdot \text{sinc}(\pi\delta f t). \quad (11)$$

The result of the fixed pixellation of the multielement modulator is now evident. The output pulse is the convolution of the input pulse not only with the desired impulse response function $h(t)$, but also with a series of replica impulse response functions, $h(t - n\delta f^{-1})$, occurring at times $t = n\delta f^{-1}$. The entire result is weighted by a temporal window function, $\text{sinc}(\pi\delta f t)$, which has its first zeros at $t = \pm\delta f^{-1}$. This exact form of the temporal envelope function arises from our assumption that the spot size w_o is very small compared to the pixel size. If we take into account the finite size of w_o in our experiments, (10) is multiplied by a second Gaussian temporal envelope function of the form $\exp(-w_o^2 t^2/8\alpha^2)$. [32] For the values of α and w_o given above, we find that the width of the Gaussian envelope function is comparable to that of the sinc-function envelope. Thus, the replica pulses as $t = \pm\delta f^{-1}$ should be present, though with somewhat reduced intensity, whereas replica pulses at larger times will be suppressed due to the fast rolloff of the Gaussian. In any case, we learn from (10) that if $h(t)$ is nonzero only during a time interval $|t| \ll \delta f^{-1}$, then the actual shaped pulse will closely approximate the desired shaped pulse, except for a few low amplitude replicas at times $t = \pm n\delta f^{-1}$. On the other hand, if $h(t)$ takes on a significant amplitude for times extending out to $|t| \sim \delta f^{-1}$, then a sort of temporal aliasing, in which the replica waveforms blend into the main waveform centered at $t = 0$, will occur.

The effect of pixellation on pulse position modulation is now analyzed by inserting

$$H(\omega) = e^{-i\omega\tau} \quad (12)$$

for the “desired frequency filtering function” in (7). The desired physical mask is

$$H(x/\alpha) = e^{-ix\tau/\alpha}. \quad (13)$$

We obtain (2) for the delay by equating τ/α , the spatial derivative of phase from (13), with $\delta\phi/\delta x$, the average spatial phase derivative imposed by the modulator: $\tau =$

$-\alpha \delta\phi/\delta x = -1/2\pi \delta\phi/\delta f$. The desired impulse response function is simply the time-shifting operation

$$h(t) = \delta(t - \tau). \quad (14)$$

Inserting into (11), we obtain the actual output pulse:

$$e_{\text{out}}(t) = \sum_n e_{\text{in}}(t - \tau - n \delta f^{-1}) \text{sinc}(\pi \delta f t). \quad (15)$$

In order to illustrate the effects of pixellation, $|e_{\text{out}}(t)|^2$, from (15), is plotted in Fig. 10 for four different values of τ , corresponding to $\delta\phi = 0, -\pi/4, -\pi/2$, and $-3\pi/4$, respectively. For $\delta\phi = -\pi/4$, corresponding to $\tau = 1.37$ ps, the pixellation has very little effect on the pulse position modulation. $\delta\phi = 0$, for which there is no time shift, is shown as a reference. For increasing values of $\delta\phi$, the main shifted pulse begins to lose intensity, and a series of replica pulses, separated by $\delta\tau = 1/\delta f = 10.87$ ps, begin to increase in intensity. At $\delta\phi = -3\pi/4$ the intensity of the main peak has dropped to 61% of its original value, and the largest replica pulse has grown to 22% of the original peak intensity. For $\delta\phi = -\pi$ (not shown), the intensity of the strongest replica pulse at $\tau = -5.4$ ps is equal to the intensity of the shifted pulse at $\tau = 5.4$ ps. In this extreme case a positive phase ramp with $\delta\phi = \pi$ cannot be differentiated from a negative phase ramp with $\delta\phi = -\pi$. Therefore, by symmetry, two equal shifted pulses at $\tau = \pm 5.4$ ps occur.

C. Programmable Chirping and Pulse Compression

Gray-level phase control can be used to achieve programmable compression of chirped optical pulses. In the spectral domain, linearly chirped optical pulses exhibit a phase response that varies quadratically with frequency. By use of the multielement modulator to compensate for the quadratic phase shift, linearly chirped pulses can be compressed down to the bandwidth limit. Compression of linearly chirped pulses is most commonly achieved, of course, by using a pair of diffraction gratings [28], [33]. Programmable compression, by using a multielement phase modulator within a pulse shaping apparatus, makes it possible to adjust the magnitude and the sign of the phase sweep electronically, without moving parts. Furthermore, the multielement modulator can also be programmed to compensate for cubic, higher order, and arbitrary spectral phase variations. Cubic phase variations, for example, arise in pulse compression below 10 fs [34] and in ultrashort pulse propagation in fibers at the so-called zero-dispersion wavelength [35].

Quadratic Phase Compensation: We now discuss the use of the multielement modulator to generate or compensate pure quadratic spectral phase shifts. We begin by establishing the connection between the chirp in the time domain and the phase shift in the frequency domain. Consider a frequency-swept pulse of the form

$$e(t) = a(t) e^{i\omega_0 t} e^{i\omega' t^2/2} \quad (16)$$

where $a(t)$ is a real function and ω_0 is a center optical frequency. The instantaneous frequency ω_{inst} is given by

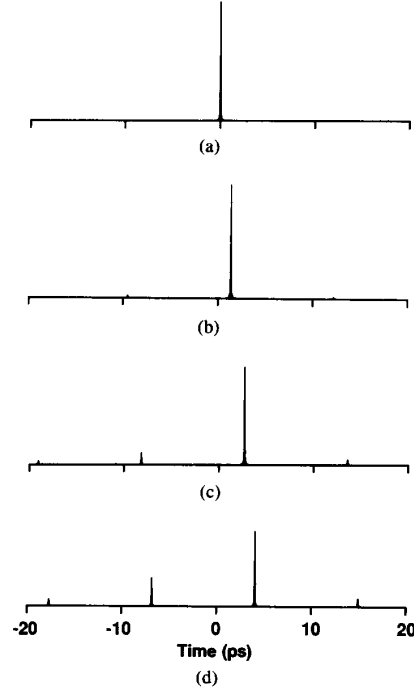


Fig. 10. Theoretical intensity profiles of temporally shifted pulses resulting from femtosecond pulse position modulation. (a) $\delta\phi = 0$. (b) $\delta\phi = -\pi/4$. (c) $\delta\phi = -\pi/2$. (d) $\delta\phi = -3\pi/4$.

the derivative of phase with respect to time, i.e., $\omega_{\text{inst}} = \omega_0 + \omega' t$. The spectrum $E(\omega)$ can be written as follows:

$$E(\omega) = A(\omega) * \exp\left(\frac{-i(\omega - \omega_0)^2}{2\omega'}\right). \quad (17)$$

Thus, $E(\omega)$ is the convolution of $A(\omega)$, the Fourier transform of the real pulse envelope $a(t)$, with a quadratic phase shift term. We can now identify the quadratic phase shift in the time domain, $\exp(i\omega' t^2/2)$, which corresponds to a linear frequency sweep at a rate $d\omega_{\text{inst}}/dt = \omega'$, with the quadratic phase shift in the frequency domain, $\exp(-i(\omega - \omega_0)^2/2\omega')$. In order to use the multielement modulator to compress a linearly chirped pulse, the individual pixels should be set to provide a quadratic phase shift equal and opposite to that of the incident pulses. This is achieved if

$$\phi_n = \delta\phi \left(n - \frac{N}{2}\right)^2 \quad (18)$$

where ϕ_n is the phase of the n th pixel, $\delta\phi = 2\pi^2 \delta f^2 / \omega'$, N is the number of pixels, and δf is the frequency change from one pixel to the next, as before. Conversely, if an unchirped pulse is incident on the pulse shaper, then the phase shift given by (18) will impose a chirp corresponding to $d\omega_{\text{inst}}/dt = -\omega'$.

In order for the multielement modulator to produce the desired result, the chirped waveform must fit within a temporal window $|t| \leq 1/2 \delta f$ due to the fixed modulator pixel size, as discussed in Section IV-B. A pulse with a

bandwidth $N \delta f$, corresponding to the full aperture of the modulator, with a phase shift given by (18), would occupy a time window $|t| \leq \pi N \delta f / \omega'$. Together these conditions require $|\delta\phi| \leq \pi/N$ in (18). This implies that the maximum permissible change in phase from one modulator element to the next is approximately π (which occurs at the edges of the modulator).

In order to demonstrate programmable pulse compression, we moved one of the gratings in the pulse shaper with respect to the lens pair. This introduces temporal dispersion [28], which results in a chirped and broadened output pulse. By using the phase modulator to compensate for the dispersion, the output pulse is restored to its original duration. An example of the data is shown in Fig. 11. A cross-correlation measurement of the original pulse, which has a duration of 83 fs, is plotted in Fig. 11(a). The chirped waveform which results when the grating is moved 2.28 cm closer to lens pair is shown in Fig. 11(b). The pulse is broadened to roughly 3 ps with a rather flat top. The calculated chirp rate is $\omega' = 2.15 \times 10^{25} \text{ s}^{-2}$; therefore $\delta\phi = 7.76 \times 10^{-3} \text{ rad}$ should be required for compensation. Fig. 11(c) shows the compressed pulse which results when the multielement modulator is set for a quadratic phase sweep with $\delta\phi = 7.73 \times 10^{-3} \text{ rad}$. The pulse is compressed back to a duration of 89 fs, with no observable pulse distortion—a compression ratio approaching $40\times$. These data demonstrate the ability to perform programmable pulse compression with extremely high fidelity.

Cubic Phase Distortion: A spectral phase variation which is cubic in frequency leads to a complicated, non-symmetric pulse distortion in the time domain. A cubic phase variation corresponds to a quadratic chirp—i.e., the arrival time of a particular frequency depends quadratically on the offset from the center frequency. In the time domain, the main effects are the appearance of a long oscillatory tail together with a broadening of the initial pulse. The oscillatory tail arises because particular frequencies above and below the center frequency can arrive at the same time and interfere. The oscillatory tail can either lead or follow the main (initial) pulse, depending on the sign of the cubic phase variation. Cubic phase variation can be especially important when ultrashort pulses propagate in optical fibers at the zero-dispersion wavelength. In more precise language, the zero-dispersion wavelength is the wavelength at which quadratic dispersion is zero—i.e., fiber propagation is unaccompanied by a phase variation quadratic in frequency. Therefore, at this wavelength cubic phase variation is the leading effect limiting linear pulse propagation in fibers. A detailed discussion of ultrashort pulse propagation in fibers in the vicinity of the zero dispersion wavelength is given by [35].

We have utilized the multielement phase modulator to impose cubic phase variations on ultrashort input pulses. The form of the phase variation is given by

$$\phi_n = \delta\phi \left(n - \frac{N}{2} \right)^3 \quad (19)$$

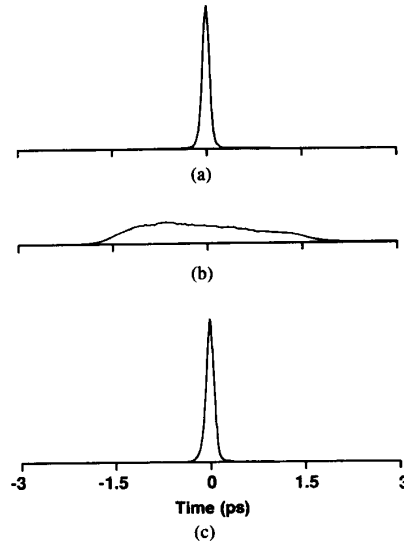


Fig. 11. Cross-correlation traces demonstrating programmable pulse compression. (a) Original 83 fs pulse. (b) Chirped waveform obtained by moving one grating 2.28 cm closer to the lens pair in the pulse shaper. (c) Compressed pulse.

where ϕ_n and $\delta\phi$ are the phase of the n th pixel and the amplitude of the phase sweep, respectively. As in the previous sections, the maximum permissible phase variation is set by the requirement that the spectrum be adequately sampled by the fixed modulator pixels. Therefore, the largest permissible phase jump from one pixel to the next is π , corresponding to a maximum delay of $\pm 1/2 \delta f = \pm 5.4 \text{ ps}$. These considerations imply that $\delta\phi$ in (20) should satisfy $|\delta\phi| \leq 4\pi/3N^2$. With $N = 128$, $|\delta\phi|$ should be less than $2.56 \times 10^{-4} \text{ rad}$.

Fig. 12 shows intensity cross-correlation measurements illustrating the effects of cubic phase distortion. Because $\delta\phi = -2.51 \times 10^{-4}$ for the Fig. 12(a) while $\delta\phi = 2.51 \times 10^{-4}$ for Fig. 12(b), the oscillatory tail follows the main pulse in 12(a) but precedes the main pulse in 12(b). In addition to the oscillatory tail, which is clearly evident and which is spread over a duration of nearly 5 ps, a broadening and a shift of the main pulse are also evident. In order to depict these effects clearly, cross-correlation measurements of undistorted incident pulses are also plotted as a basis for comparison.

Fig. 12(c) shows the theoretical intensity profile of an 85 fs initial pulse after distortion by a cubic phase sweep with $\delta\phi = -2.51 \times 10^{-4}$. The theoretical plot is in good qualitative agreement with the data in Fig. 12(a). All the essential features of the data, including the approximate duration and oscillation period of the tail, as well as the broadening and shift of the principal peak, are evident in the simulation. There are some discrepancies concerning the details of the oscillatory tail; in particular, the data exhibit less regularity and a shallower modulation compared to the theory. A decrease in the modulation depth of the tail can be caused by deviations from an exact cubic spectral phase variation [24]. Thus, the slight discrepan-

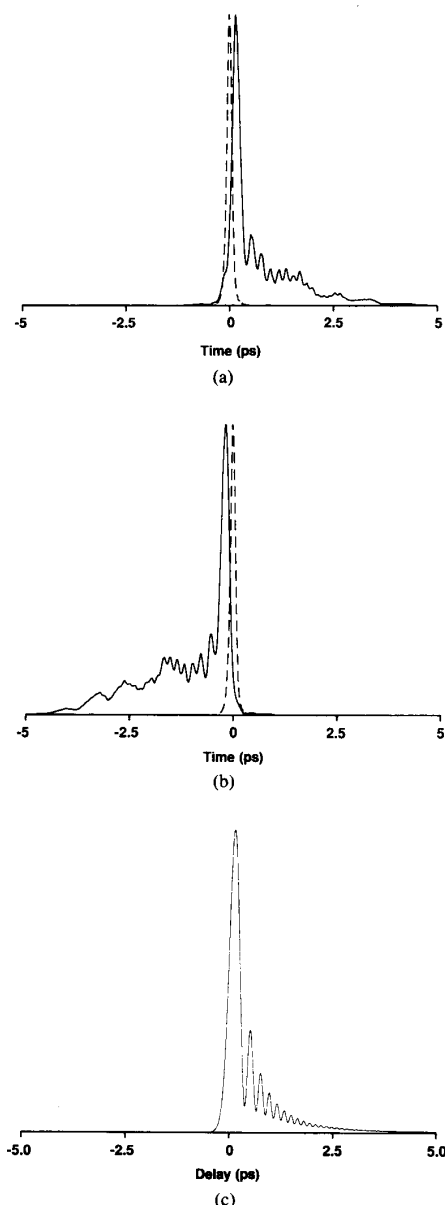


Fig. 12. (a), (b) Cross-correlation traces of pulses distorted by cubic spectral phase variations with (a) $\delta\phi = -2.51 \times 10^{-4}$ and (b) $\delta\phi = 2.51 \times 10^{-4}$. The dotted line shows the cross-correlation of the incident undistorted pulse for comparison. (c) Theoretical intensity profile corresponding to data in (a) above.

cies between theory and experiment may be an indication of slight inaccuracies in controlling the phases of individual modulator elements.

We comment briefly on an alternative technique for imposing or compensating cubic phase variations, based on the use of a deformable mirror within a pulse shaping apparatus [24]. The setup for this approach is similar to the one considered in the present paper, except that a deformable mirror, which is specially designed to assume a pure cubic shape with an adjustable amplitude, is used in place

of the multielement modulator. Advantages of the deformable mirror cubic phase mask include simplicity and the ability to generate large and very accurate cubic phase variations. Advantages of the present multielement modulator approach include easy tuning of the amplitude and sign of the phase variation as well as the flexibility to compensate for arbitrary phase variations.

V. CONCLUSION

In summary, we have demonstrated programmable shaping of femtosecond optical pulses by using a 128-element liquid crystal phase modulator. Refinements in the design of the modulator provide for excellent pulse shaping fidelity and a high spectral resolution which were previously available only with microlithographically-fabricated masks. Furthermore, the use of the multielement modulator makes possible continuously variable phase control which is not readily available with fixed masks and which is required in order to generate arbitrarily shaped pulses.

Most importantly, our work demonstrates the use of multielement modulators to achieve high quality programmable pulse shaping. In addition to the liquid crystal phase modulator used in the current paper, other types of multielement modulators, such as multielement amplitude modulators, could also be used to obtain different functionalities. The speed at which pulse shapes can be reprogrammed is set by the speed of the modulator array; therefore, the use of a faster modulator array, perhaps utilizing electrooptic or optoelectronic technology, could make possible reconfigurable pulse shaping on a nanosecond time scale. The ability to design, synthesize, and modulate ultrafast optical waveforms according to specification should have widespread applications in ultrafast nonlinear optics and ultrafast optical communications.

ACKNOWLEDGMENT

It is a pleasure to acknowledge J. Heritage for providing the theoretical plot of cubic phase distortion shown as Fig. 12(c) and L. Carrion for constructing the driver circuit.

REFERENCES

- [1] C. Froehly, B. Colombeau, and M. Vampouille, "Shaping and analysis of picosecond light pulses," in *Progress in Optics*, E. Wolf, Ed. Amsterdam: North-Holland, 1983, vol. 20, pp. 115-121.
- [2] J. P. Heritage, A. M. Weiner, and R. N. Thurston, "Picosecond pulse shaping by spectral phase and amplitude manipulation," *Opt. Lett.*, vol. 10, p. 609, 1985.
- [3] A. M. Weiner, J. P. Heritage, and J. A. Salehi, "Encoding and decoding of femtosecond pulses," *Opt. Lett.*, vol. 13, p. 300, 1988.
- [4] A. M. Weiner, J. P. Heritage, and E. M. Kirschner, "High-resolution femtosecond pulse shaping," *J. Opt. Soc. Amer.*, vol. B5, p. 1563, 1988.
- [5] M. Haner and W. S. Warren, "Generation of programmable, picosecond-resolution shaped laser pulses by fiber-grating pulse compression," *Opt. Lett.*, vol. 12, p. 398, 1987.
- [6] M. Haner and W. S. Warren, "Generation of arbitrarily shaped picosecond optical pulses using an integrated electro-optic waveguide modulator," *Appl. Phys. Lett.*, vol. 52, p. 1458, 1988.

- [7] T. Kobayashi and A. Morimoto, "Electro-optical synthesis of picosecond optical pulses," in *OSA Proc. Picosecond Electron. Optoelectron.*, T. C. L. G. Sollner and D. M. Bloom, Eds., Washington, DC: Opt. Soc. Amer., 1989, p. 81.
- [8] J. A. Salehi, A. M. Weiner, and J. P. Heritage, "Coherent ultrashort light pulse code-division multiple access communication systems," *J. Lightwave Technol.*, vol. 8, p. 478, 1990.
- [9] A. M. Weiner, J. P. Heritage, R. J. Hawkins, R. N. Thurston, E. M. Kirschner, D. E. Leaird, and W. J. Tomlinson, "Experimental observation of the fundamental dark soliton in optical fibers," *Phys. Rev. Lett.*, vol. 61, p. 2445, 1988.
- [10] A. M. Weiner, R. N. Thurston, W. J. Tomlinson, J. P. Heritage, D. E. Leaird, E. M. Kirschner, and R. J. Hawkins, "Temporal and spectral self-shifts of dark optical solitons," *Opt. Lett.*, vol. 14, p. 868, 1989.
- [11] W. S. Warren, "Effects of pulse shaping in laser spectroscopy and nuclear magnetic resonance," *Science*, vol. 242, p. 878, 1988.
- [12] A. M. Weiner, Y. Silberberg, H. Fouckhardt, D. E. Leaird, M. A. Saifi, M. J. Andrejco, and P. W. Smith, "Use of femtosecond square pulses to avoid pulse breakup in all-optical switching," *IEEE J. Quantum Electron.*, vol. 25, p. 2648, 1989.
- [13] S. Maneuf and F. Reynaud, "Quasi-steady state self-trapping of first, second and third order subnanosecond soliton beams," *Opt. Commun.*, vol. 66, p. 325, 1988.
- [14] Y.-X. Yan, E. B. Gamble, and K. A. Nelson, "Impulsive stimulated scattering: General importance in femtosecond laser interactions with matter, and spectroscopic applications," *J. Chem. Phys.*, vol. 83, p. 5391, 1985.
- [15] S. Shi, A. Woody, and H. Rabitz, "Optimal control of selective vibrational excitation in harmonic linear chain molecules," *J. Chem. Phys.*, vol. 88, p. 6870, 1988.
- [16] A. M. Weiner, D. E. Leaird, G. P. Wiederrecht, and K. A. Nelson, "Femtosecond pulse sequences used for optical control of molecular motion," *Science*, vol. 247, p. 1317, 1990.
- [17] J. P. Heritage, A. M. Weiner, and R. N. Thurston, "Fourier transform picosecond pulse shaping and spectral phase measurements in a grating pulse-compressor," in *Ultrafast Phenomena V*, G. R. Fleming and A. E. Siegman, Eds., Berlin: Springer, 1986, pp. 33-37.
- [18] J. L. A. Chilla and O. E. Martinez, "Direct determination of the amplitude and the phase of femtosecond light pulses," *Opt. Lett.*, vol. 16, p. 39, 1991.
- [19] A. M. Weiner and D. E. Leaird, "Generation of terahertz-rate trains of femtosecond pulses by phase-only filtering," *Opt. Lett.*, vol. 15, p. 51, 1990.
- [20] V. A. Bogatyrev, M. M. Bubnov, E. M. Dianov, A. S. Kurkov, P. V. Mamyshev, S. I. Miroshnichenko, S. D. Romyantsev, V. A. Semeonov, S. L. Semeonov, A. A. Sysoliatin, and S. V. Chernikov, "Experimental generation of 0.2 THz fundamental soliton train in a fiber with varying dispersion," in *Tech. Dig. Series. Nonlinear Guided Wave Phenomena: Physics and Applications*, vol. 2, Washington, DC: Opt. Soc. Amer., 1989, paper PD-9.
- [21] J. P. Heritage, R. N. Thurston, W. J. Tomlinson, A. M. Weiner, and R. H. Stolen, "Spectral windowing of frequency-modulated optical pulses in a grating compressor," *Appl. Phys. Lett.*, vol. 47, p. 87, 1985.
- [22] J. P. Heritage, A. M. Weiner, R. J. Hawkins, and O. E. Martinez, "Stabilized pulse compression by multiple-order stimulated raman scattering with group velocity dispersion," *Opt. Commun.*, vol. 67, p. 367, 1988.
- [23] R. L. Fork, "Optical frequency filter for ultrashort pulses," *Opt. Lett.*, vol. 11, p. 629, 1986.
- [24] J. P. Heritage, E. W. Chase, R. N. Thurston, and M. Stern, "A simple femtosecond optical third-order disperser," presented at CLEO, Baltimore, MD, 1991.
- [25] P. J. Delfyett, J. P. Heritage, E. W. Chase, and R. N. Thurston, "Femtosecond pulse generation by cubic phase compensation in semiconductor traveling wave amplifiers," presented at CLEO, Baltimore, MD, 1991.
- [26] A. M. Weiner, D. E. Leaird, J. S. Patel, and J. R. Wullert, "Programmable femtosecond pulse shaping by use of a multielement liquid-crystal phase modulator," *Opt. Lett.*, vol. 15, p. 326, 1990.
- [27] J. A. Valdmanis, R. L. Fork, and J. P. Gordon, "Generation of optical pulses as short as 27 femtoseconds directly from a laser balancing self-phase modulation, group-velocity dispersion, saturable absorption, and saturable gain," *Opt. Lett.*, vol. 10, p. 131, 1985.
- [28] O. E. Martinez, "3000 times grating compressor with positive group velocity dispersion: Application to fiber compensation in 1.3-1.6 μm region," *IEEE J. Quantum Electron.*, vol. QE-23, p. 59, 1987.
- [29] P. G. deGennes, *The Physics of Liquid Crystals*. Oxford, Clarendon, 1974.
- [30] F. S. Lonberg, R. B. Meyer, "New ground state for the splay-fredericksz transition in a polymer nematic liquid crystal," *Phys. Rev. Lett.*, vol. 55, p. 718, 1985.
- [31] J. E. Rothenberg, D. Grischkowsky, and A. C. Balant, "Observation of the formation of the 0π pulse," *Phys. Rev. Lett.*, vol. 53, p. 552, 1984.
- [32] R. N. Thurston, J. P. Heritage, A. M. Weiner, and W. J. Tomlinson, "Analysis of picosecond pulse shape synthesis by spatial masking in a grating pulse compressor," *IEEE J. Quantum Electron.*, vol. QE-22, p. 682, 1986.
- [33] E. B. Treacy, "Optical pulse compression with diffraction gratings," *IEEE J. Quantum Electron.*, vol. QE-5, p. 454, 1969.
- [34] R. L. Fork, C. H. Brito Cruz, P. C. Becker, and C. V. Shank, "Compression of optical pulses to six femtoseconds by using cubic phase compensation," *Opt. Lett.*, vol. 12, p. 483, 1987.
- [35] M. Stern, J. P. Heritage, and E. W. Chase, "Grating compensation of third-order fiber dispersion," submitted to *IEEE J. Quantum Electron.*



Andrew M. Weiner (S'84-M'84-SM'91) was born in Boston, MA, on July 25, 1958. He received the S.B., S.M., and Sc.D. degrees in electrical engineering from the Massachusetts Institute of Technology, Cambridge, in 1979, 1981, and 1984, respectively. From 1979 through 1984, he was a Fannie and John Hertz Foundation Graduate Fellow. His doctoral thesis, for which he was awarded a 1984 Fannie and John Hertz Foundation Doctoral Thesis Prize, dealt with femtosecond pulse compression and measurement of femtosecond dephasing in condensed matter.

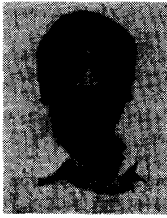
In 1984 he joined Bellcore, Red Bank, NJ, where he has conducted research on shaping of ultrashort optical pulses, optical probing of picosecond electronics, all-optical switching, and ultrafast nonlinear optics in fibers. His current research interests center on applications of femtosecond pulse shaping to femtosecond spectroscopy, and nonlinear optics. Since 1989, he has been District Manager of Ultrafast Optics and Optical Signal Processing Research.

Dr. Weiner is an Associate Editor of this JOURNAL and of *Optics Letters*. In 1988-1989, he was an IEEE Lasers and Electro-Optics Society Traveling Lecturer, and in 1990 he received the Adolph Lomb Award of the Optical Society of America. He has served on the program committee of several conferences and was Vice Chairman of the 1989 Gordon Conference on Nonlinear Optics and Lasers. In 1990-1991, he was Chair of the Ultrafast Phenomena Technical Group of the Optical Society of America. He is also a Fellow of the Optical Society of America.



Daniel E. Leaird was born in Muncie, IN, on December 4, 1964. He received the B.S. degree in physics from Ball State University, Muncie, IN, in 1987.

He joined Bellcore, Red Bank, NJ, in 1987 as a member of the Ultrafast Optics and Optical Signal Processing Research group. His current work is in the field of femtosecond optics and pulse shaping.



J. S. Patel received the Ph.D. degree from the State University of New York at Stony Brook in 1982. His thesis work was centered around electric field effects in molecular solids.

In 1982 he joined Bell Laboratories as a post-Doctoral member of technical staff. He was made a regular member of the technical staff at AT&T Bell Laboratories in 1984. In 1987 he joined Bellcore where he has continued his work on liquid crystals. He has made significant contributions in understanding the structure of liquid crystals at microscopic and macroscopic levels and discovered new electrooptic effects such as flexoelectric effect in cholesteric liquid crystals and the anomalous electroclinic effect in smectics. He has also made major contributions in understanding surface interactions of liquid crystals and developed techniques for controlling the surface interactions. Several of these advances have been used to make novel liquid crystal devices that have been used

for communications, optical neural networks, and for optical information processing.



John R. Wullert II received the B.S. degree from Lafayette College, Easton, PA, in 1984 and the M.S. degree from Carnegie Mellon University, Pittsburgh, PA, in 1986, both in electrical engineering.

He joined Bellcore in 1986 and since that time has been involved with various aspects of information display research. His current interest is in modulators and materials for optical computing and signal processing.

Mr. Wullert is a member of the Institute of Electrical and Electronic Engineers, the Optical Society of America, and the Society for Information Display.